

# ERIKA: Emulating Retarding-field-energy-analyzer Ion Kinetic-transport in Argon-gas

Felipe Soberon<sup>a)</sup>

(Dated: 31 March 2023)

This document reports a one-dimensional simulation of the transport of argon ions across a plasma sheath and through a retarding field energy analyzer (RFEA). The simulation can model DC and AC sheaths. The DC sheath is modeled using Child Law and the AC sheath using the analytical solution of a radio-frequency capacitive sheath by M. A. Lieberman. The model includes elastic and charge exchange ion collisions with background Argon gas.

Keywords: Plasma sheath, Child Law, RF sheath, Charge exchange collision, Retarding Field Energy Analyzer (RFEA)

## I. INTRODUCTION

Retarding field analyzers are employed to assess the energy distribution of ions impinging on a surface. Ions acquire considerable kinetic energy as a result of the high voltage across the plasma sheath. This energy distribution is valuable in various applications, such as space propulsion equipment. In other contexts, such as the manufacturing of semiconductor devices, plasma etching equipment, or plasma deposition, the ion energy serves as a parameter that can influence the etch rate, the profile of the process, or the deposition rate.

RFEA devices can be designed as an array of thin grids tightly packed together, with a series of voltages applied to these grids. The primary purpose of this configuration is to select ions based on their energy and to eliminate the detection of electrons originating from the plasma discharge or secondary electrons emitted by the RFEA following ion impact.

The operational range of RFEA devices is limited by several factors, including background gas pressure, fast electrons from the plasma, secondary electrons emitted within the RFEA, ionization occurring inside the RFEA, the distance between RFEA grids, and field distortion within the RFEA caused by space charge.

To assess the impact of any of the factors mentioned above, a computer simulation of a plasma sheath and RFEA grid would enable one to explore these factors individually or in combination.

Here we report a one-dimensional model of a plasma sheath and RFEA device.

## II. SIMULATION DESCRIPTION

In this section we provide details of the model. Subsection II.A describe how the space potential and electric field are calculated including the plasma sheath and in the RFEA region. Subsection II.B describe the method to integrate the ion trajectories under the effect of the fields described in subsection II.A. Subsection II.C describes the method to simulate ion collisions with the background gas.

### II.A. Space Potential and Electric Field

The space potential and electric field are calculated in two regions: the RFEA region, and the plasma sheath. The model is one-dimensional, therefore only space potential and electric field in the  $z$ -axis is calculated in these regions. In this geometry, the RFEA is located at  $z \leq 0$  and its extension in the negative direction of the  $z$ -axis depends on the spaces between the grids and the collector; subsection II.A.1. The plasma sheath starts at  $z = 0$  and extends to the plasma, which is located at some  $z_{\text{plasma}} > 0$ . The location of the plasma sheath boundary edge depends on the plasma sheath model and is further described in subsection II.A.2.

#### II.A.1. Retarding Field Energy Analyzer

The RFEA modeled includes the standard four grids and collector plate<sup>1</sup>. These are identified as  $G_0$ ,  $G_1$ ,  $G_2$ ,  $G_3$ ,  $C$ . The first grid,  $G_0$ , faces the plasma and is at the same potential as the electrode that bounds the plasma discharge. In this model, the voltage of  $G_0$  is set to zero. The second grid,  $G_1$  is typically biased negative respect to  $G_0$  to repel electrons from the plasma discharge. The model does not include electrons, however, this grid is included to simulate the electric field that affects the motion of ions between  $G_0$  and  $G_1$ . The third grid,  $G_2$ , is used to discriminate ions by setting the voltage of  $G_2$  positive relative to  $G_0$ . The voltage of  $G_2$  is typically swept from zero to a large voltage to limit the ion current to the collector and generate the RFEA characteristic voltage-current curve. The fourth grid,  $G_3$ , is used to repel secondary electrons that may be emitted by the collector due to ion impact. This grid is usually biased slightly negative relative to the voltage applied to the collector. Again, the model does not include electrons, however, it is included to simulate the electric field between  $G_3$  and the collector that affect the ion trajectories. Finally, the last electrode in the RFEA is the collector,  $C$ , which is biased somewhat negative relative to the first grid,  $G_0$ .

The model assumes that the grids and non-

dimensional; i.e. zero thickness. This differs from actual RFEA devices where the grids are usually 40  $\mu\text{m}$  thick (reference some publication by Impedans). Consequently, the model also neglects any lensing effects of non-zero thick grids<sup>2,3</sup>. The distance between grids and the collector are defined in the model as multiples of 100  $\mu\text{m}$ . In actual RFEA devices the grids are physically separated by sheets of Mica, 100  $\mu\text{m}$  thick each sheet. The arrangement of grids and spacers is known as the RFEA button stack. For instance, the standard RFEA button stack of a commercial device comprises two spacers between  $G_0$  and  $G_1$ , three spacers between  $G_1$  and  $G_2$ , three spacers between  $G_2$  and  $G_3$ , and two spacers between  $G_3$  and the collector C (reference impedans website Semion). This arrangement is therefore known as a 2332 button stack. The model can simulate the RFEA with any combination of button stack arrangements expressed as multiples of the basic spacer.

Besides lensing effects, not included in this model, actual grids are not entirely transparent and a fraction of ions moving through the RFEA are collected by the grids. The transparency of the grids depends on the ion energy and may vary due to the lensing effect. While the model presented here does not simulate these effects it includes a simple transparency factor setting. The user can set this number to any value from 0 to 100%. The transparency setting is common to all grids; i.e., the transparency of grids cannot be set individually.

The space potential between grids is calculated by linear interpolation. Similarly, the electric field between grids is calculated as the potential difference between each grid pair divided by the distance. Figure 1 shows the space potential and electric field in the RFEA for grid voltage settings  $G_0=0$ ,  $G_1=-60$ ,  $G_2=250$ ,  $G_3=-70$ , and  $C=-60$  V. The location of the grids and collector is indicated with vertical dashed lines.

### II.A.2. Sheath Model

The space potential and electric field in the sheath region of the plasma is determined from the Child Law sheath model for direct-current sheath<sup>4</sup>, and from the analytical solution of capacitive radio-frequency sheath for alternate-current sheath<sup>5,6</sup>. These Child Law solutions are collisionless and therefore not valid when the background pressure of neutral argon is high. Therefore this limits the model simulating pressure parameter. Nonetheless, RFEAs are most useful in low pressure plasmas where the ion energy gain is not impeded by frequent collisions and we shall limit simulations to a maximum pressure of 10 Pa (75 mTorr, 100  $\mu\text{bar}$ ). The capacitive radio-frequency solution has been reported for a collisionless regime<sup>5</sup> and a collisional regime<sup>6</sup> and, hence, the latter is used in the model as it accounts for pressure parameter. The formulae for both regimes are summarized here as they only differ by a couple of scaling parameters.

For the DC case, the Child Law sheath size is calcu-

lated

$$s_{\text{Child Law}} = \frac{\sqrt{2}}{3} \lambda_D \left( \frac{2V_0}{T_e} \right)^{3/4} \quad (1)$$

Where  $\lambda_D$  is the Debye length

$$\lambda_D = \sqrt{\frac{\epsilon_0 T_e}{en_s}} \quad (2)$$

Where  $T_e$  is the electron temperature (in eV),  $\epsilon_0$  is vacuum permittivity (in Farads/metre),  $e$  is the basic electric charge (in Coulomb), and  $n_s$  is the plasma density at the sheath edge (in  $\text{m}^{-3}$ ).

The voltage in the Child Law sheath is given by

$$V_{\text{Child Law}}(z) = V_0 \left( 1 - \left( 1 - \frac{z}{s_{\text{Child Law}}} \right)^{4/3} \right) \quad (3)$$

Where the position variable,  $z$ , is given in metres, and where  $V_0$  is the voltage of the plasma sheath edge relative to the bounding electrode at  $z = 0$ . The voltage is null at  $z = 0$  and  $V_0$  at  $z = s_{\text{Child Law}}$ . The plasma potential is positive relative to the electrode, therefore  $V_0$  is positive.

The electric field (in V/m) is given by

$$E_{\text{Child Law}}(z) = -\frac{4}{3} \frac{V_0}{s_{\text{Child Law}}} \left( 1 - \frac{z}{s_{\text{Child Law}}} \right)^{1/3} \quad (4)$$

Note the field is null at  $z = s_{\text{Child Law}}$  and negative otherwise in the sheath region.

Figure 1 shows the space potential and electric field for the DC sheath solution with a voltage across the sheath of 1000 V and plasma density  $n_s = 10^{16} \text{ m}^{-3}$ . Note that even for a small voltage at the discriminator grid  $G_2$  (relative to the plasma potential) the electric fields within the RFEA are much higher than the electric field across the sheath due to the proximity between grids; i.e., ions experience substantially higher forces within the RFEA.

The space potential and electric field for the AC sheath are calculated using the capacitive sheath solution of Lieberman<sup>5,6</sup>. The sheath edge of the capacitive radio-frequency discharge changes through the cycle, from collapsing when the voltage across the sheath drops to its minimum to full expansion when the voltage is maximum. The size of the sheath is given by,

$$s(\phi) = s_0(1 - \cos(\phi) + \frac{H}{8} \{ \frac{3}{2} \sin(\phi) + \frac{11}{18} \sin(3\phi) - 3\phi \cos(\phi) - \frac{1}{3} \phi \cos(3\phi) \}) \quad (5)$$

With  $\phi = \omega t$  ( $\omega = 2\pi f$ ) and  $f$  the radio-frequency. The value of  $s(t)$  is limited to  $\phi$  in the range from 0 ( $t = 0$ ) to  $\pi$  ( $t = T/2$ ; where  $T = 1/f$  is the radio-frequency cycle period). The size of the sheath at  $t = 0$  is zero and its maximum size at  $s(t = T/2) = s_m$ . The  $s(t)$  function can be evaluated at any time value via the following

$$s(t) = \text{abs}(s(\omega\tau(t))) \quad (6)$$

$$\tau(t) = \text{remainder} \left( t + \frac{T}{2}, T \right) - \frac{T}{2} \quad (7)$$

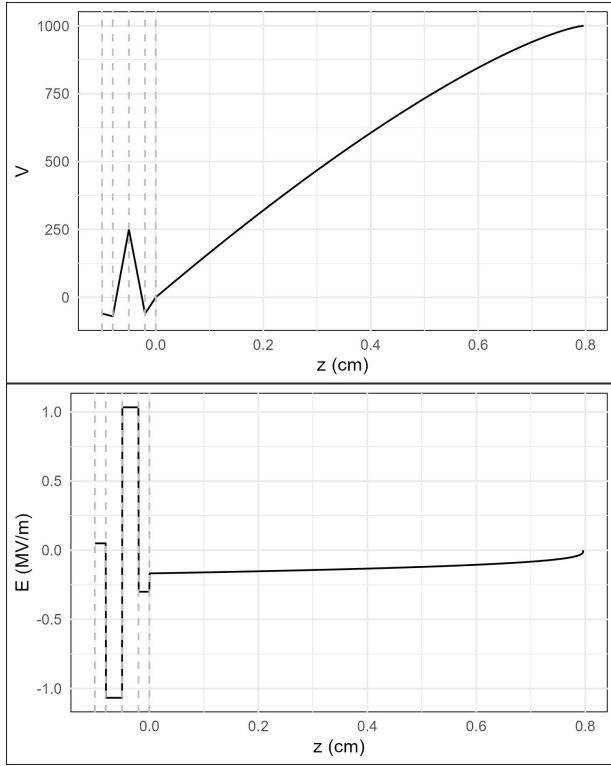


FIG. 1 Space potential across a plasma sheath and RFEA grid stack (top) and corresponding electric field (bottom) for DC plasma sheath with a voltage across the sheath of 1000 V. The edge of the plasma sheath and plasma is at  $z = 0.8$  cm. The RFEA is located at  $z \leq 0$ ; with the plasma facing grid ( $G_0$ ) at  $z = 0$ . The location of the RFEA grids and collector are indicated by vertical dashed lines.

The parameter  $s_0$  is given by

$$s_0 = \frac{J}{en_s\omega} \quad (8)$$

$J$  is the total current through the plasma discharge (mainly displacement current in the sheaths and conduction current in the plasma bulk). The current can be calculated from the plasma density at the sheath edge ( $n_s$ ), the maximum voltage across the sheath ( $V_0$ ), the radio-frequency and the electron temperature in the collisionless regime solution<sup>5</sup>

$$J = \frac{2\omega}{5} \sqrt{\frac{2}{5}} \sqrt{en_s\epsilon_0} \sqrt{\sqrt{3T_e} \sqrt{192T_e + 125V_0} - 24T_e} \quad (9)$$

In the case of the collisional regime solution it is not possible to solve analytically the plasma discharge current. Instead, the maximum voltage across the sheath can be expressed in terms of the current and other plasma parameters<sup>6</sup>

$$V_0 = \frac{Js_0}{\epsilon_0\omega} \left( 2 + \frac{125}{192} H\pi \right) \quad (10)$$

Where the expression for  $H$  is given later in this section. The inverse expression,  $J(V_0)$ , can be solved numerically. In the simulation program, 64 pairs  $(V_0(J), J)$  for  $J$  from

0 to 500 A/m<sup>2</sup> are generated. The value of  $J$  is determined by linear interpolation of the two nearest pairs.

The  $H$  parameter for the collisionless regime is given by<sup>5</sup>

$$H = \frac{1}{\pi} \frac{s_0^2}{\lambda_D^2} \quad (11)$$

And in the collisional regime is given by<sup>6</sup>

$$H = \sqrt{\frac{2\lambda_i s_0}{\pi^2 \lambda_D^2}} \quad (12)$$

Where  $\lambda_i$  is the ion mean free path (in m). This parameter is estimated for argon gas by<sup>6</sup>

$$\lambda_i = (30p/0.13332237)^{-1} \quad (13)$$

With  $p$  the neutral argon gas pressure in Pascal. The ion mean free path is assumed to be constant, i.e., independent of the ion energy, for the purpose of the sheath solution<sup>6</sup>. For similar discharge current and radio-frequency voltage, the effect of ion collisions in the sheath is to reduce the size of the plasma sheath<sup>6</sup>.

From here on, the sheath size, the electric field and the space potential across the sheath described below differ between the two regimes only by the scaling parameters  $H$  and  $s_0$  and the discharge current  $J$ .

The electric field in the  $z$ -direction is given by

$$E_{AC}(z, t) = \frac{J}{\epsilon_0\omega} \{ \cos(\omega t) - \cos(\phi(s_m - z)) \} \quad (14)$$

If  $s(t) < s_m - z$ , otherwise the electric field is zero. Note that the function  $\phi(s)$  is the inverse of the sheath size  $s(\phi)$ , that it does not have an analytical solution, and that it is numerically solved in the computer code. 64 pairs  $(s(\phi), \phi)$  for  $\phi$  from 0 to  $\pi$  in steps of  $\pi/64$  are generated. The value of  $\phi$  for a given  $s$  is determined by linear interpolation of the two nearest pairs.

Finally, the space potential for the capacitive radio-frequency sheath is given by the integral

$$V_{AC}(z, t) = \int_0^z E_{AC}(\xi, t) d\xi \quad (15)$$

With  $z$  in the range from  $z = 0$  to  $z = s_m$ . The field is numerically integrated.

The space potential and electric field for the AC sheath solution, with set pressure 0.5 Pa, are shown in Fig. 2. The curves plotted show both results at times 0,  $T/4$  and  $T/2$ . Note that at  $T/2$  the voltage across the sheath is null and there is no electric field acting on the ions. This modulation affects the ion motion; this is illustrated in the next subsection.

Other sheath models can be found in the literature. Davis and Vanderslice reported a DC sheath model with a linearly varying electric field and compared with ion energy measurements<sup>7</sup>. Wild and Koidl reported an AC sheath model and simulated ion energy distributions and experimental IEDF results in a reverse asymmetric capacitive plasma discharge driven at 13.56 MHz with excellent agreement between model and experimental results<sup>8</sup>. Robiche et al. reported a capacitive radio frequency sheath solution for two a plasma driven at two

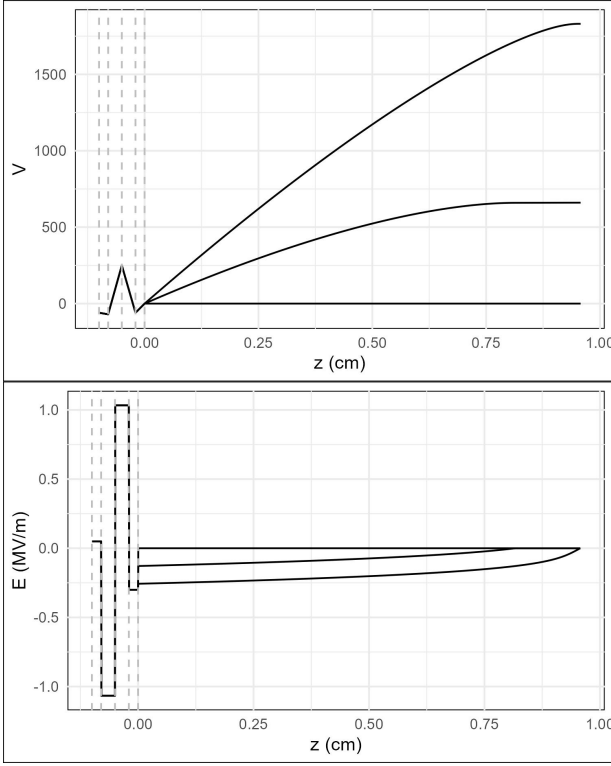


FIG. 2 Space potential across a plasma sheath and RFEA grid stack (top) and corresponding electric field (bottom) for AC sheath solution with maximum voltage across the sheath of 2000 V. Potential and field curves are shown for time  $t = 0$ ,  $T/4$ , and  $T/2$ . The sheath is fully expanded at  $t = 0$ , at  $z > 1$  cm.

frequencies<sup>9</sup>, i.e., a dual-frequency solution counterpart to the single frequency solution of Lieberman<sup>5</sup>.

## II.B. Ion trajectory integration

The ion trajectories under the force of the electric field in the sheath region and the RFEA region is integrated with a Runge-Kutta algorithm of fourth order. The integration time step is set to  $dt = 100$  ps. This time step is sufficiently small, i.e. an ion will have to reach a velocity of 1000 km/s to travel  $100 \mu\text{m}$  (the thickness of an RFEA stack spacer) in time  $dt$ . The starting position for every ion is the sheath edge,  $z = s_{\text{Child Law}}$  for the DC case, and the position of the fully expanded sheath in the AC case ( $z = s_m$ ). All ions start with velocity equal to the Bohm velocity in the direction of the bounding electrode.

$$v_z = -v_{\text{Bohm}} = -\sqrt{\frac{eT_e}{M_{\text{Ar}}}} \quad (16)$$

Where  $M_{\text{Ar}}$  is the mass of the argon atom/ion.

The ion flux is therefore,

$$\Gamma_0 = en_s v_{\text{Bohm}} \quad (17)$$

Fig. 3 shows a sample collisionless ion trajectory under the effect of the AC field of Fig. 2. Note the step increments in velocity corresponding to the modulation of the electric field in the sheath. Once in the RFEA region,

the ion accelerates and decelerates according to the grid potentials. The ion in this case has enough energy to make it to the collector.

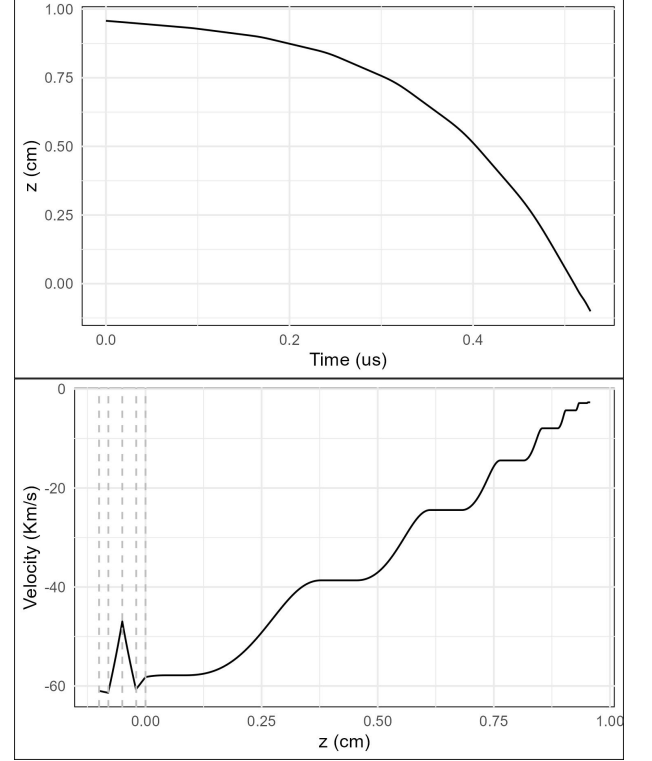
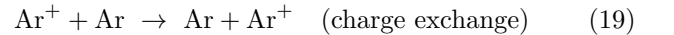
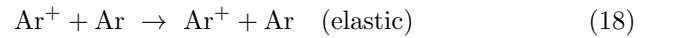


FIG. 3 Collisionless sample trajectory of an argon ion from the plasma edge, through the plasma sheath and the RFEA for the AC sheath case of Fig. 2. The top plot shows the position of the ion in the  $z$  axis in time and the bottom plot shows the velocity of the ion in the  $z$  direction as a function of position in  $z$ .

## II.C. Collisions of ions with background gas

Ion collisions are modelled using cross sections for two types of collisions



The cross sections for these two processes can be found in the LXCat database<sup>10</sup>. The set for Ar ions was reported by Phelps<sup>11</sup>. The isotropic collision cross section data set is used to model elastic collisions, and the backscattering collision cross section data is used to model charge exchange collisions. Except at very low energies, the charge exchange collision cross section is larger than the elastic collision cross section and therefore is the predominant collision process between argon ions and background argon gas (Fig. 4). Furthermore, charge exchange collision can change the forward velocity of the ion whereas elastic collisions are predominantly small-angle scattering<sup>7</sup>.

The model assumes that the predominant ion species in the plasma discharge is  $\text{Ar}^+$ . It has been reported that double charge ions, i.e.,  $\text{Ar}^{++}$ , have a smaller cross section than the single charge ions and therefore have an

average energy closer to the maximum potential energy across the sheath<sup>7</sup>. Hence, the ion energy distribution in a highly ionized plasma would differ from those distributions reported here.

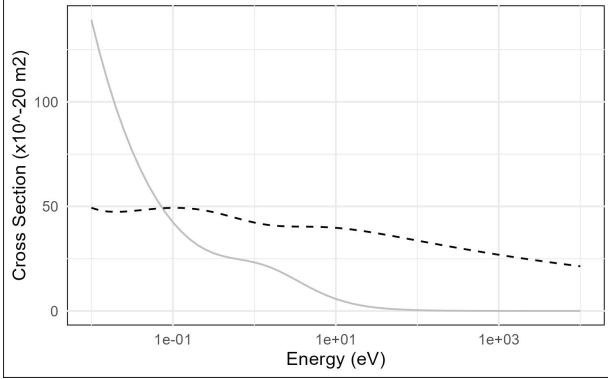


FIG. 4 Cross sections for elastic (gray curve) and charge exchange collisions (dashed curve) for argon ion collisions with background argon gas<sup>10,11</sup>.

The probability of a collision at every time step is approximated by

$$P_{\text{col}} = \nu(\varepsilon)dt \quad (20)$$

$$\nu(\varepsilon) = n_{\text{gas}}\sigma(\varepsilon)v_{\text{Ar}^+} \quad (21)$$

Where  $\nu(\varepsilon)$  is the collision rate ( $\text{s}^{-1}$ ),  $n_{\text{gas}}$  is the density of neutral argon gas,  $\sigma(\varepsilon) = \sigma_{\text{el}}(\varepsilon) + \sigma_{\text{cx}}(\varepsilon)$  is the total cross section (function of the ion energy), and  $v_{\text{Ar}^+}$  is the velocity magnitude of the argon ion. A random number is generated in the code every time step and if it is smaller than the probability of a collision then the ion velocity is modified according to one of the two processes. To determine which process to apply a second random number is generated and compared to

$$P_{\text{el}} = \frac{\sigma_{\text{el}}(\varepsilon)}{\sigma_{\text{el}}(\varepsilon) + \sigma_{\text{cx}}(\varepsilon)} \quad (22)$$

If the random number is smaller than  $P_{\text{el}}$  then the collision is taken as elastic, otherwise it is charge exchange type.

The elastic collision is processed as follows. First, a neutral argon atom is given a velocity vector in three-dimensional space with magnitude equal to the mean average velocity (at 300 K) pointing in a random direction using random numbers to generate azimuth and polar angles. Second, the reference frame is changed from the laboratory reference frame to the neutral argon atom reference frame. Third, the reference frame is rotated in the z-x plane to point in the direction that makes the argon ion parallel to the rotated z-axis. Fourth, a random number is used to generate a random scattering angle (between 0 and  $\pi/2$ ) and to update the ion velocity vector. Fifth, the ion the reference frame is rotated back. Sixth, the reference frame is changed back to the laboratory reference frame.

The charge exchange collision is processed as follows. First, a neutral argon atom is given a velocity vector

in three-dimensional space with magnitude equal to the mean average velocity (at 300 K) pointing in a random direction using random numbers to generate azimuth and polar angles. Second, this velocity is assigned to the argon ion.

Fig. 5 shows the trajectory of an ion in an AC field (Fig. 2) with a collision event (charge exchange). The effect of the collision is the loss of the energy gained by the ion from the edge of the plasma up to the z position of the collision event. This type of collisions combined with the AC modulation of the sheath lead to complex ion energy distribution with multiple-peak structure<sup>8</sup>.

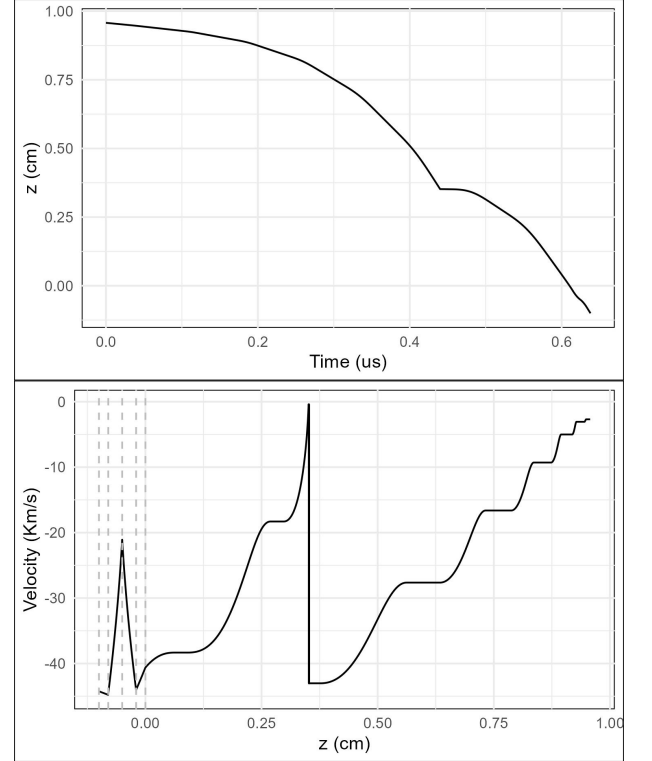


FIG. 5 Sample trajectory of an argon ion including a collision event. The sheath is AC driven and the potential and field are those shown in Fig. 2

### III. RESULTS

In this section we present results of running the simulation described in the previous section. The subsections below focus on the following research questions,

- How well does the RFEA derived ion energy distribution function represents the actual energy distribution function of ions at the bounding electrode (i.e., at  $G_0$ )?
- What is the effect of ion space charge inside the RFEA on the space potential and electric field?
- What is the effect of different spacings between grids on the RFEA derived ion energy distribution function when compared to the actual one at the bounding electrode?

### III.A. Ion energy distribution profile

First, we run the simulation at various pressures and compared the derived ion energy distribution function with the actual energy distribution as recorded in the model at  $G_0$ . The RFEA configuration is as follows: 2332 stack,  $G_1=C=-60$  V,  $G_3=-70$  V, grid transparency 100 %. The plasma sheath potential used is AC with maximum voltage difference across the sheath of 2000 V (i.e.,  $V_{pk-pk}$ ), the radio-frequency 13.56 MHz, and the plasma density  $10^{16} \text{ m}^{-3}$ . The pressure settings are 0.5, 1.0, 2.0, 5.0, 7.5 and 10.0 Pa. The model is run sweeping grid  $G_2$  voltage setting from 0 to 1500 V in steps of 25 V. The number of ions whose trajectory is simulated per  $G_2$  voltage step is 25000. The starting time for each ion is randomized uniformly across the radio-frequency period to represent that ions may enter the sheath at any point during the RF cycle. Each ion trajectory is followed for a total time of 1  $\mu\text{s}$ .

Figure 6 shows the characteristic current-voltage curve for each model RFEA scan. The vertical axis is the ion count at the collector position. The ion count drops as the pressure is increased.

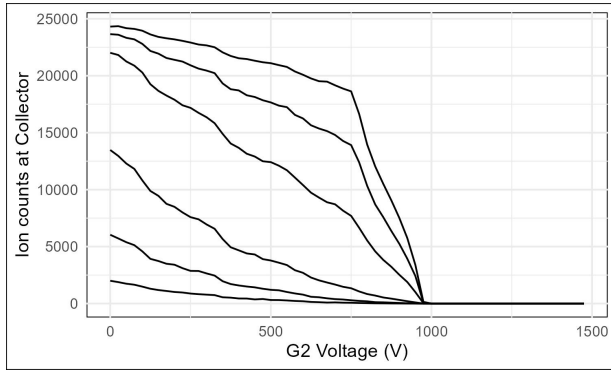


FIG. 6 Current-voltage characteristic curves where the current is represented by the ion count collected at the collector position. The curves from highest ion count value to lowest correspond to pressure settings from 0.5 to 10.0 Pa.

The first derivative of the ion current is proportional to the ion energy distribution function<sup>1</sup>. The set of curves on the left of Figure 7 shows the first derivative of the curves in Figure 6. The derivatives are normalized and plotted with an offset in the vertical axis from lowest pressure setting at the top to highest pressure setting at the bottom. The ion energy distributions derived from the ion counts at the collector in the simulated RFEA for the various pressure settings can be contrasted with the actual ion energy distributions recorded at  $G_0$ , before the ions transport through the RFEA. These IEDFs are shown on the right of Figure 7. These scan were repeated with using a smaller integration time step,  $dt = 10$  ps, to assess any potential artifact introduced in the simulation by the trajectory integration method. No substantial qualitative difference on the energy distribution functions was observed (not shown). The derived IEDF at the collector exhibits more noise than the IEDF at  $G_0$  due to

the nature of the numerical derivative of the collector ion count; i.e., numerical derivatives of any parameter always amplifies the parameter's noise. Here, a centered finite difference method was used to differentiate the Collector ion counts. All curves are shown without any smoothing.

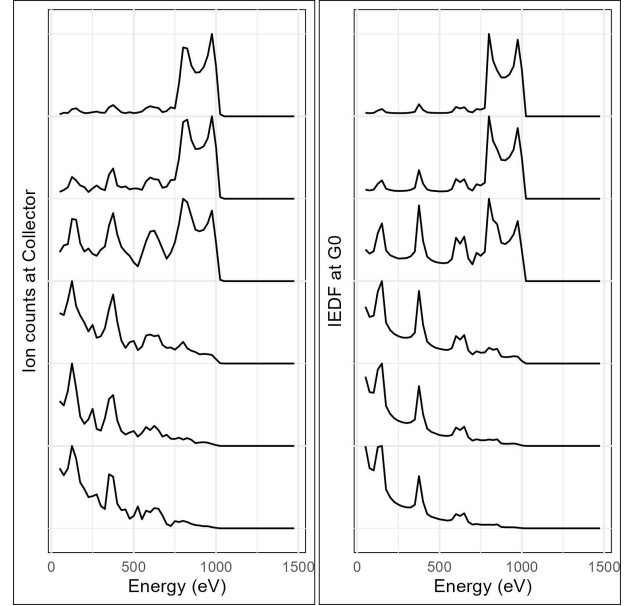


FIG. 7 Ion energy distribution functions. Left: First derivative of the current-voltage characteristic curves of Figure 6. Right: Plot of the ion energy distribution as recorded in the simulation at  $G_0$ , before ion transport through the RFEA. Both set of curves are normalized. The curves from top to bottom correspond to pressure settings from 0.5 to 10.0 Pa.

The ion energy distributions of Figure 7 exhibit a series of peaks which are the result of the oscillating plasma sheath and ion collisions with the background gas. More specifically, the sheath modulation, i.e., the time varying sheath edge and sheath electric field, can shape specific features of the IEDFs<sup>8,12</sup>.

<sup>a</sup>)Impedans Ltd.; Electronic mail: felipe.soberon@impedans.com; <http://www.impedans.com>

<sup>1</sup>I. H. Hutchinson, *Principles of plasma diagnostics* (Cambridge University Press, 1987).

<sup>2</sup>T. H. M. van de Ven, C. A. de Meijere, R. M. van der Horst, M. van Kampen, V. Y. Banine, and J. Beckers, "Analysis of retarding field energy analyzer transmission by simulation of ion trajectories," *Review of Scientific Instruments* **89**, 043501 (2018).

<sup>3</sup>J. W. Buijter, *Functional analysis of retarding field energy analyzers for ion energy distribution measurements in plasma enhanced atomic layer deposition*, Ph.D. thesis, Eindhoven University of Technology (2018).

<sup>4</sup>M. A. Lieberman and A. J. Lichtenberg, *Principles of plasma discharges and materials processing*, 2nd ed. (Wiley, 2005).

<sup>5</sup>M. A. Lieberman, "Analytical solution for capacitive rf sheath," *IEEE Transactions on Plasma Science* **16**, 638–644 (1988).

<sup>6</sup>M. A. Lieberman, "Dynamics of a collisional, capacitive rf sheath," *IEEE Transactions on Plasma Science* **17**, 338–341 (1989).

<sup>7</sup>W. D. Davis and T. A. Vanderslice, "Ion energies at the cathode of a glow discharge," *Physical Review* **131**, 219–228 (1963).

<sup>8</sup>C. Wild and P. Koidl, "Ion and electron dynamics in the sheath of radio-frequency glow discharges," *Journal of Applied Physics* **69**, 2909–2922 (1991).

- <sup>9</sup>J. Robiche, P. C. Boyle, M. M. Turner, and A. R. Ellingboe, “Analytical model of a dual frequency capacitive sheath,” *Journal of Physics D: Applied Physics* **36**, 1810–1816 (2003).
- <sup>10</sup>“Lxcat database,” <http://www.lxcat.net>.
- <sup>11</sup>A. V. Phelps, “The application of scattering cross sections to ion flux models in discharge sheaths,” *Journal of Applied Physics* **76**, 747 (1994).
- <sup>12</sup>C. Wild and P. Koidl, “Structured ion energy distribution in radio frequency glow-discharge systems,” *Applied Physics Letters* **54**, 505–507 (1989).
- <sup>13</sup>B. Bohm and J. Perrin, “Retarding-field analyzer for measurements of ion energy distributions and secondary electron emission coefficients in low-pressure radio frequency discharges,” *Review of Scientific Instruments* **64**, 31–44 (1993).
- <sup>14</sup>S. Ries, M. Schroeder, M. Woestefeld, C. Corbella, I. Korolov, P. Awakowicz, and J. Schulze, “Relative calibration of a retarding field energy analyzer sensor array for spatially resolved measurements of the ion flux and ion energy in low temperature plasmas,” *Review of Scientific Instruments* **92**, 103503 (2021).
- <sup>15</sup>K. Denieffe, C. M. O. Mahony, P. D. Maguire, D. Gahan, and M. B. Hopkins, “Retarding field energy analyser ion current calibration and transmission,” *Journal of Physics D: Applied Physics* **44**, 075205 (2011).
- <sup>16</sup>T. Baloniak, R. Reuter, C. Flotgen, and A. von Keudell, “Calibration of a miniaturized retarding field analyzer for low-temperature plasmas: geometrical transparency and collisional effect,” *Journal of Physics D: Applied Physics* **43**, 055203 (2010).
- <sup>17</sup>S. Sharma, D. Gahan, P. Scullin, S. Daniels, and M. B. Hopkins, “Ion angle distribution measurement with a planar retarding field analyzer,” *Review of Scientific Instruments* **86**, 113501 (2015).
- <sup>18</sup>S. Sharma, D. Gahan, S. Kechkar, S. Daniels, and M. B. Hopkins, “A spatially resolved retarding field energy analyzer design suitable for uniformity analysis across the surface of a semiconductor wafer,” *Review of Scientific Instruments* **85**, 043509 (2014).
- <sup>19</sup>M. Haass, M. Darnon, G. Cunge, O. Joubert, and D. Gahan, “Silicon etching in a pulsed hbr/o<sub>2</sub> plasma. i. ion flux and energy analysis,” *Journal of Vacuum Science and Technology B* **33**, 032202–1 (2015).
- <sup>20</sup>W. J. Goedheer, “Lecture notes on radio-frequency discharges, dc potentials, ion and electron energy distributions,” *Plasma Sources Science and Technology* **9**, 507–516 (2000).
- <sup>21</sup>L. F. Velasquez-Garcia, J. Izquierdo-Reyes, and H. Kim, “Review of in-space plasma diagnostics for studying the earth’s ionosphere,” *Journal of Physics D: Applied Physics* **55**, 263001 (2022).